

Multiscale Simulation Method for Quantitative Prediction of Surface Wettability at the Atomistic Level

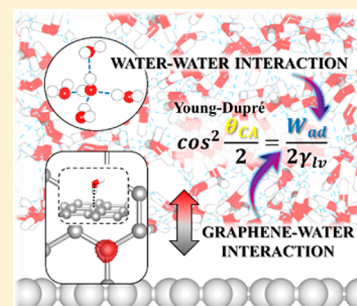
Suji Gim,[†] Hyung-Kyu Lim,^{*,‡} and Hyungjun Kim^{*,†}

[†]Department of Chemistry and Graduate School of EEWS, Korea Advanced Institute of Science and Technology (KAIST), Yuseong-gu, Daejeon 34141, Korea

[‡]Department of Chemical Engineering, Kangwon National University, Chuncheon, Gangwon-do 24341, Korea

S Supporting Information

ABSTRACT: The solid–liquid interface is of great interest because of its highly heterogeneous character and its ubiquity in various applications. The most fundamental physical variable determining the strength of the solid–liquid interface is the solid–liquid interfacial tension, which is usually measured according to the contact angle. However, an accurate experimental measurement and a reliable theoretical prediction of the contact angle remain lacking because of many practical issues. Here, we propose a first-principles-based simulation approach to quantitatively predict the contact angle of an ideally clean surface using our recently developed multiscale simulation method of density functional theory in classical explicit solvents (DFT-CES). Using this approach, we simulate the surface wettability of a graphene and graphite surface, resulting in a reliable contact angle value that is comparable to the experimental data. From our simulation results, we find that the surface wettability is dominantly affected by the strength of the solid–liquid van der Waal's interaction. However, we further elucidate that there exists a secondary contribution from the change of water–water interaction, which is manifested by the change of liquid structure and dynamics of interfacial water layer. We expect that our proposed method can be used to quantitatively predict and understand the intriguing wetting phenomena at an atomistic level and can eventually be utilized to design a surface with a controlled hydrophobic(philic)ity.



The concept of wettability, i.e., the degree of spreading water over the solid surface, has been applied to regulate various chemo-physical reactions in the fields of water harvesting,¹ self-cleaning,² corrosion,³ filtration,⁴ heterogeneous catalytic reaction,^{5,6} etc. Despite its critical importance in a number of practical applications, fundamental characterizations and understanding on the wetting phenomena at the molecular level remain lacking. Moreover, an accurate measurement of the contact angle (θ_{CA}) is often difficult to accomplish because of defects,⁷ airborne contaminants,⁸ and oxide layer formation⁹ on the surface. In the case of thin film systems, their intrinsic surface corrugation adds more complications because the surface geometry is another influential element on the surface energy.

Even for a graphite surface that is chemically much more inert than other surfaces, e.g., metals, experimental measurement on the water contact angle substantially varies. In 1940, Fowkes et al. reported the θ_{CA} of 86° that is measured using the tilting plate method.¹⁰ Using the rising meniscus method, Morcos reported the similar value of 86° in 1972.¹¹ However, Tadros et al. measured a rather low value of 60–80° using the captive bubble method in 1974.¹² An even lower value of $42 \pm 7^\circ$ was estimated by Schrader in 1980,⁷ and $<30^\circ$ was obtained from a scanning force microscopy study by Luna et al.¹³ In addition, there still is much debate regarding the influence of possible contaminants during experimental measurements.⁸

As a complement to experiments, in such cases, first-principle-based simulation can serve as the most reliable method to provide a theoretical bound for predicting the θ_{CA} values of idealized surface by minimizing all possible ambiguities at the atomic scale. On the basis of quantum mechanics (QM), density functional theory (DFT) rather accurately describes the noncovalent interaction between the solid surface and a liquid molecule, particularly with the recent development of various van der Waal's corrected DFT methods.^{14–19} However, because of its high computational cost, DFT calculations are often conducted in a static manner while ignoring the dynamics; as a result, the liquid phase cannot be properly considered. When the dynamics is included in DFT, a formidable computational cost of *ab initio* molecular dynamics (AIMD) simulations hampers a sufficient sampling of molecular configurations of the liquid phase.

In this regard, classical molecular dynamics (MD) simulations have often been employed to investigate the surface wetting properties. Driskill et al.²⁰ simulated the contact angle on graphene sheets using the semi-infinite cylindrical drop model and Raj et al.,²¹ and Shih et al.²² investigated the wettability of graphene using a spherical nanodroplet method. These methods require not only extrapolation to an increase in

Received: February 12, 2018

Accepted: March 20, 2018

Published: March 20, 2018

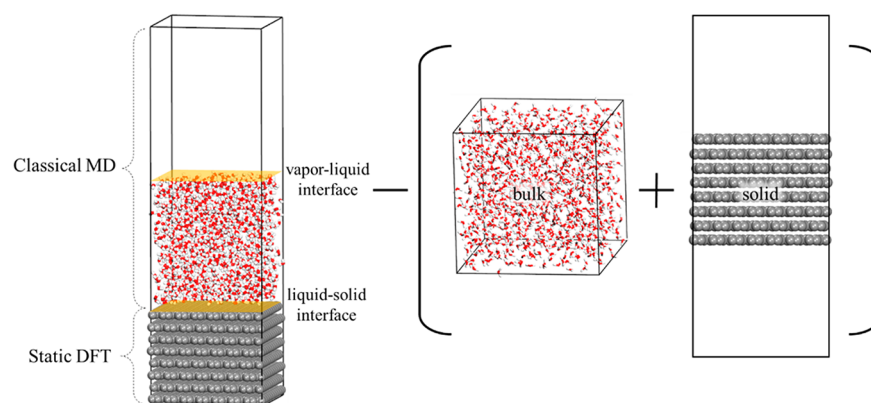


Figure 1. Schematic diagram of the simulation cell of solid (graphite)–liquid (water) interface (left) and the definition of reference states (right) to define the interfacial free energies. The sum of two interfacial free energies regarding the solid–liquid interface, and the liquid–vapor interface is calculated by subtracting the (free) energy of bulk water and the solid slab from the total free energy of the solid–liquid interfacial system. Carbon, oxygen, and hydrogen are denoted as gray, red, and white dots, respectively.

droplet size to eliminate line tension effects but also a certain degree of arbitrariness to define the boundary of the droplet.^{23,24} In addition, in classical MD simulations, the solid–liquid interaction energy is heavily dependent on the choice of force-field (FF) parameters.^{25–27} Thus, without any input from experiments, the quantitative prediction of the surface wettability is usually unavailable using classical MD simulations.

In this paper, we propose a multiscale approach for a quantitative prediction of surface wettability. Using our recently developed multiscale simulation method, DFT in classical explicit solvents (DFT-CES),²⁸ we simulated the solid surface using a DFT and used a classical MD for the liquid phase. Within the DFT-CES framework, we propose a systematic strategy to develop reliable van der Waals (vdW) parameters that can transfer the accurate description of the “single water–surface” interaction (which can be derived from accurate QM calculations) to the description of the “liquid water–surface” interfacial interaction. We then apply our multiscale method to investigate a graphene/graphite–water interface and provide a quantitative theoretical bound of water contact angle of graphite as well as full atomistic details regarding the interface, such as hydrogen bond network and water structure nearby graphene/graphite.

Multiscale Simulation Method: DFT-CES. The DFT-CES method is a mean-field self-consistent quantum mechanics/molecular mechanics (QM/MM) method.²⁸ By completely decoupling the time scales of two different levels, QM particles experience the mean electrostatic potential (MESP) of MM particles as an external potential, while MM particles experience the MESP of QM particles as an external potential. To describe the interfacial interaction within reasonable computational efficiency, the MESP of QM particles is approximated by the electrostatic potential calculated from the static DFT optimization, $V_{\text{QM}}^{\text{ES}}$, while removing QM particle dynamics. The MESP of MM particles, $\langle V_{\text{MM}}^{\text{ES}} \rangle$, is calculated using the time average of the classical MD simulation trajectories. Thus, modified QM and MM Hamiltonians can be expressed as

$$H_{\text{QM}} = H_{\text{QM}}^0 + \langle V_{\text{MM}}^{\text{ES}} \rangle \quad (1)$$

$$H_{\text{MM}} = H_{\text{MM}}^0 + E_{\text{int}}^{\text{vdW}} + E_{\text{int}}^{\text{ES}} \quad (2)$$

where H_{QM}^0 and H_{MM}^0 are quantum and classical Hamiltonians with no external potential (i.e., with no coupling with MM at H_{QM}^0 and with no coupling with QM at H_{MM}^0), respectively. $E_{\text{int}}^{\text{vdW}}$ is the vdW interaction at the interface between QM and MM particles; this interaction relies on a pairwise FF-type description. $E_{\text{int}}^{\text{ES}}$ is the electrostatic interaction energy between MM point charges and “QM nuclei + electron density” given by $E_{\text{int}}^{\text{ES}} = \sum_{\mu \in \{\text{MM particles}\}} q_{\mu} V_{\text{QM}}^{\text{ES}}$.

DFT-CES employs a real-space grid as a communication channel for the electrostatic interactions, where $V_{\text{QM}}^{\text{ES}}$ is stored from the DFT simulation and transferred to the MD simulation. In addition, $V_{\text{MM}}^{\text{ES}}$ is an averaged 3D grid potential sampled from the MD simulation and then transferred to DFT simulation. Finally, both Hamiltonians of eqs 1 and 2 are solved until a self-consistent solution is obtained. Full details regarding the method and implementation are described in one of our past publications.³⁰

Calculation of Contact Angle. Using the DFT-CES method, we can simulate the semi-infinite interface between a solid slab and a liquid slab, as illustrated in Figure 1, where the solid part is simulated using a static DFT and the liquid part is simulated using a classical MD. After consecutive iterations of DFT and MD, we can obtain the mean-field solution of the solid–liquid interface, along with the final DFT energetics and MD trajectories.

We first formally define the entire free energy (A_{tot}) of the solid–liquid interfacial system as

$$A_{\text{tot}} = -k_{\text{B}}T \ln \int d\mathbf{r}^n d\mathbf{p}^n \langle \Psi | \exp\{-\beta H_{\text{tot}}\} | \Psi \rangle \quad (3)$$

where $H_{\text{tot}} = H_{\text{QM}}^0 + H_{\text{MM}}^0 + E_{\text{int}}^{\text{vdW}} + E_{\text{int}}^{\text{ES}}$ and k_{B} and T denote the Boltzmann constant and temperature, respectively ($\beta = 1/k_{\text{B}}T$). If we employ an infinite mass approximation for QM particles, as done in our DFT-CES formalism, the phase space integration about QM and MM degrees of freedom in eq 3 is reduced into the phase space integration only about the MM degrees of freedom; $\int d\mathbf{r}^n d\mathbf{p}^n \rightarrow \int d\mathbf{r}_{\text{MM}}^n d\mathbf{p}_{\text{MM}}^n$. As H_{QM}^0 being independent of the MM degrees of freedom $\{r_{\text{MM}}^n, p_{\text{MM}}^n\}$, eq 3 is rewritten as

$$A_{\text{tot}} = A_1 + E_{\text{s}}^0 \quad (4)$$

where the first term can be referred as a free energy of the liquid part (A_1) that is under the external potential from the

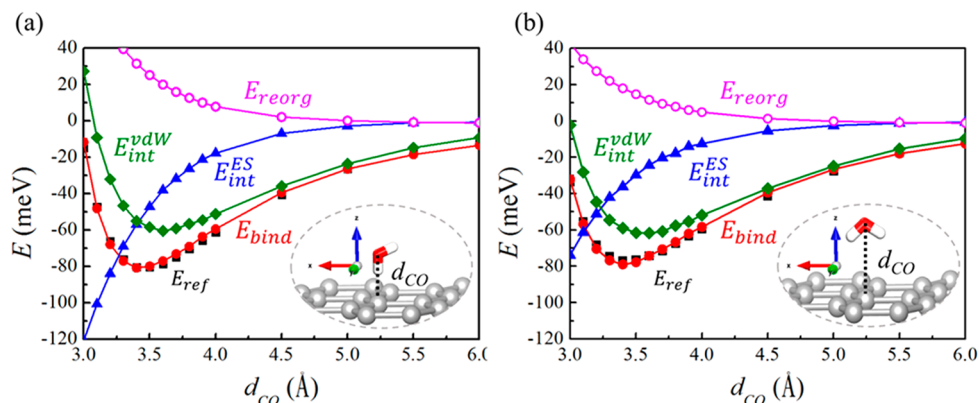


Figure 2. Single water–graphene binding energy curves calculated for two different water configurations; (a) one-leg configuration and (b) two-leg configuration. The DFT-CES total energy (E_{bind} ; red) includes the electrostatic interaction energy between the water dipole and the polarized electron of the graphene ($E_{\text{int}}^{\text{ES}}$; blue), the energetic cost to polarize the electron cloud (E_{reorg} ; magenta), and the van der Waals (vdW) interaction between the water molecule and graphene atoms ($E_{\text{int}}^{\text{vdW}}$; green). The parameters for vdW interaction are optimized to reproduce E_{ref} obtained using vdW-DF2^{C09x} functional (black), which reproduces the quantum Monte Carlo (QMC) level of binding energies.

solid part, and the second term can be referred as the internal energy of the solid part (E_s^0), which are expressed as

$$A_1 = -k_B T \ln \int d\mathbf{r}_{\text{MM}}^m d\mathbf{p}_{\text{MM}}^m \exp(-\beta H_{\text{MM}}) \quad (5)$$

$$\begin{aligned} E_s^0 &= \langle \Psi | H_{\text{QM}}^0 | \Psi \rangle = \langle \Psi | H_{\text{QM}} - \langle V_{\text{MM}}^{\text{ES}} \rangle | \Psi \rangle \\ &= E_s^{\text{DFT}} - \langle \Psi | \langle V_{\text{MM}}^{\text{ES}} \rangle | \Psi \rangle \end{aligned} \quad (6)$$

Here $E_s^{\text{DFT}} = \langle \Psi | H_{\text{QM}} | \Psi \rangle$ that is the DFT self-consistent energy, and thus E_s^0 in eq 6 can also be straightforwardly calculated by decomposing the energetics of the last DFT step of the DFT-CES self-consistent loop.

To efficiently obtain A_1 from the trajectory sampled from the last MD step of the DFT-CES self-consistent loop, we apply the two-phase thermodynamic (2PT) analysis, $A_1 = A_1^{2\text{PT}}$. This allows a fast and accurate calculation of the free energy quantities by properly approximating the entire partition function of the liquid system as the combination of two analytically solvable models: a hard-sphere model for translational and rotational diffusion part and a quasi-harmonic oscillator model for the vibrational and librational part.^{29,30} Note that the 2PT method can be used to calculate the absolute entropy values of various liquids, including water, surface tensions, etc.^{30–33} Further, when combined with DFT-CES, 2PT has successfully described the solvation free energies of 17 small organic molecules.²⁸

As a reference energy of the liquid phase, we use the free energy of bulk liquid computed using 2PT ($A_{\text{l(b)}}^{2\text{PT}}$), which can be calculated from an additional MD simulation for the 3D periodic liquid box. As a reference energy of the solid phase, we use the DFT energy of the solid slab *in vacuo*, $E_s^0 = \langle \Psi^0 | H_{\text{QM}}^0 | \Psi^0 \rangle$, which can be calculated using DFT, where the superscript ‘0’ denotes the quantities in the absence of liquid external potential, i.e., *in vacuo*. Next, because of the existence of two different interfaces, as illustrated in Figure 1, the relative energy of solid–liquid system with respect to the aforementioned reference systems becomes the sum of the solid–liquid interfacial free energy, A_{sl} , and the liquid–vacuum interfacial free energy, A_{lv} . This leads to

$$A_{\text{sl}} = A_{\text{tot}} - (A_{\text{l(b)}}^{2\text{PT}} + E_s^0) - A_{\text{lv}} \quad (7)$$

Because A_{lv} is an extensive quantity that linearly increases as the interfacial area S increases, we obtain a linear curve of A_{lv} versus S by independently performing several sets of MD simulations of liquid slabs with different surface areas. Using the predetermined linear curve, we determine A_{lv} for a given S . Next, since the separating process of the liquid from the solid slab involves the formation of another liquid–vapor interface, the work of adhesion is simply given as $W_{\text{ad}} = (A_{\text{lv}} - A_{\text{sl}})/S$, and the value of θ_{CA} can be calculated using the Young–Dupré equation:³⁴

$$\cos \theta_{\text{CA}} = \frac{W_{\text{ad}}}{\gamma_{\text{lv}}} - 1 \quad (8)$$

where γ_{lv} is the surface tension of the liquid with respect to vacuum.

Computational Details of DFT-CES. In this study, we investigated the water on graphene/graphite system. We performed DFT-CES calculations by using Quantum Espresso³⁴ and Large-scale Atomic/Molecular Massively Parallel Simulator (LAMMPS)³⁸ to solve quantum and classical Hamiltonians, respectively, and merging the results. For the DFT part, we calculated from a single to eight graphene layers, each consisting of 24 carbon atoms with dimensions of 8.55 Å × 7.41 Å. We chose the Perdew–Burke–Ernzerhof (PBE) exchange–correlation functional,³⁵ and electron–ion interactions were considered in the form of the projector-augmented-wave (PAW) method³⁶ with a plane-wave up to an energy cutoff of 600 eV. For the classical MD part, we used the (4 × 4) expanded supercell structure of the DFT simulation cell to minimize the finite size effect during MD sampling. We noted that the $\langle V_{\text{MM}}^{\text{ES}} \rangle$ sampled using the expanded cell is folded into the smaller DFT cell when it is plugged into the quantum Hamiltonian in eq 1. We simulated 1000 water molecules, for which intermolecular interaction is described using either the SPC/E force field³⁹ or the TIP3P-Ew force field.⁴² The long-range interaction was treated using the multilevel summation method (MSM) to apply the periodic boundary condition (PBC) only along the x - and y -directions (the z -direction was chosen as the surface normal direction with open boundary condition), where the real-space cutoff was set as 12 Å. We set the MD time step as 1 fs, and we performed a canonical ensemble (NVT) MD simulation at 300 K for 1 ns, where the

sampled trajectory for the last 500 ps was employed to compute $\langle V_{\text{MM}}^{\text{ES}} \rangle$.

We performed consecutive DFT-MD cycles until the internal energy change of the solid part became less than 0.002 Ry.

Water Monomer Binding to Graphene. To obtain the reference energy curve for the “single water-graphene” interaction in Figure 2, we performed DFT calculations using vdW-DF2 with the modified exchange functional of C09x for two different orientations of water molecule.³⁷ In agreement with the previous report,⁴¹ we found that only vdW-DF2^{C09x} reproduces the accurate binding energy of 80.41 meV and distance of 3.5 Å for one-leg configuration, and the binding energy of 76.52 meV and distance of 3.5 Å for two-leg configuration, which are comparable to quantum Monte Carlo (QMC) values (-70 ± 10 meV at 3.4–4.0 Å),⁴⁰ whereas other vdW-corrected DFT methods predict overbinding tendency (Figure S1). Unsurprisingly, PBE underestimates the binding curve because of the insufficient description of the vdW interaction.

In the context of DFT-CES energetics, we also investigated the binding process of a classical water molecule to a quantum mechanically described graphene monolayer. For given fixed charges of the FF description on the water molecule, it is noted that the graphene electron density is polarized upon the response of the dipolar field of the water molecule (Figure S2). This invokes an increase of internal energy of the graphene part because of the electronic reorganization upon the external dipolar field of MM charges, E_{reorg} , and a nonzero electrostatic attraction between a water molecule and a graphene with a polarized electron density, $E_{\text{int}}^{\text{ES}}$ both of which contribute to the entire binding energy. Thus, the vdW interaction between a water molecule and graphene, $E_{\text{int}}^{\text{vdW}}$, is described using a typical 12–6 Lennard-Jones (LJ) function between the O atom of the water molecule and the C atom of the graphene; this interaction is the other contribution to the binding energy. We thus considered the single water binding energy to the graphene surface as $E_{\text{bind}} = E_{\text{reorg}} + E_{\text{int}}^{\text{ES}} + E_{\text{int}}^{\text{vdW}}$ in DFT-CES and optimized the associated LJ parameters in $E_{\text{int}}^{\text{vdW}}$ (which are ϵ_{CO} for the well depth and σ_{CO} for the effective diameter) to reproduce the binding energy curve from the vdW-DF2^{C09x} calculations.

Table 1 shows the optimized LJ parameters for carbon and oxygen at the graphene–water interface. Regardless of the

Table 1. Van der Waal’s (vdW) Parameters between a Graphene Carbon Atom and a Water Oxygen Atom (ϵ_{CO} and σ_{CO}) Optimized to Reproduce an Accurate Binding Curve of the Single Water Binding to a Graphene Monolayer Using DFT-CES^a

	SPC/E	TIP3P-Ew
ϵ_{CO}	0.078	0.078
σ_{CO}	3.547	3.547

^avdW interaction is described using 12-6 Lennard-Jones potential function, $4\epsilon_{\text{CO}}[(\sigma_{\text{CO}}/r)^{12} - (\sigma_{\text{CO}}/r)^6]$. Units are kcal/mol for ϵ_{CO} and Å for σ_{CO} .

choice of the water model between SPC/E and TIP3P-Ew, we obtained identical LJ parameters. Our results infer that an attempt to fit vdW parameters to reproduce an accurate single water binding energy without including the polarization effect of graphene π -electrons leads an overestimate of vdW interaction between liquid water and graphene. Indeed, a linear relationship between θ_{CA} and E_{bind} from ref 29, which is

empirically derived with no consideration of polarization effect, yields a fairly small value of $\theta_{\text{CA}} = 74^\circ$ (i.e., exaggerated interfacial interaction) when $E_{\text{bind}} \approx 80$ meV.

Graphene/Graphite Wettability. Using optimized vdW parameters, we perform DFT-CES simulations for the interfacial system consisting of a multilayered graphene and 1000 water molecules (Figure S3). Using the final MD trajectories, we compute the free energy of $A_{\text{l}}^{2\text{PT}}$ using 2PT analysis and calculate the total free energy of the interfacial system, A_{tot} , using eqs 4–6.

To obtain reference states energies, we performed an additional DFT calculation to obtain the energy of a graphene layer *in vacuo* (E_{s}^0) and performed an additional MD simulation of water box with 3D PBC to obtain $A_{\text{l(b)}}^{2\text{PT}}$ (Figure S4) and three sets of MD simulations of water slabs with different surface areas (S) providing a linear dependence of the water–vacuum interfacial free energy, A_{lv} , on S (Figure S5). Using E_{s}^0 and A_{lv} for a given interfacial area defined by the DFT-CES simulation cell, we obtain the solid–liquid interfacial free energy of A_{sl} from eq 7 and then calculate the work of adhesion, W_{ad} .

We find that W_{ad} is calculated to be 73.74 mN/m for the graphene interface with 1000 SPC/E waters and 74.27 mN/m for the graphene interface with 1000 TIP3P-Ew waters; these values are almost identical to each other. It should be noted that the slope of A_{lv} versus S , which is the calculated surface tension of water (49.43 mN/m for SPC/E and 36.43 mN/m for TIP3P-Ew), shows a rather substantial deviation from the experimental value (72.8 mN/m). This result implies that the error originating from the incompleteness of the FF description can be successfully removed by subtracting the calculated value of A_{lv} from the calculated value of A_{tot} in eq 4. This allows the calculated W_{ad} to become nearly independent of the choice of FF.

Consequently, when we convert the calculated W_{ad} into the contact angle value of θ_{CA} using the Young–Dupré equation, we employ an experimental surface tension value of 72.8 mN/m, which is denoted as γ_{lv} in eq 8. For the graphene–water interface, we obtain $\theta_{\text{CA}} = 88.6^\circ$ and 88.2° when using SPC/E and TIP3P-Ew models, respectively.

By increasing the number of graphene layer, we also calculate the change of W_{ad} and θ_{CA} (Figure 3). As the number of graphene layers increases, we find the increase of W_{ad} along

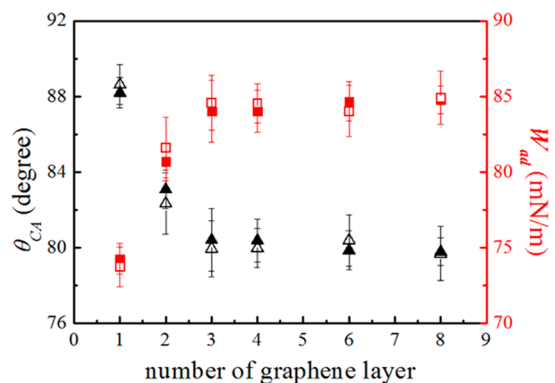


Figure 3. Change of contact angle (θ_{CA} ; black) and work of adhesion (W_{ad} ; red) as a function of number of graphene layers. The empty marks are from the SPC/E water model, and the filled marks are from TIP3P-Ew model; virtually no difference is found between the results of these models. The error bar is the standard deviation estimated by analyzing 50 independent sets of MD simulation trajectories.

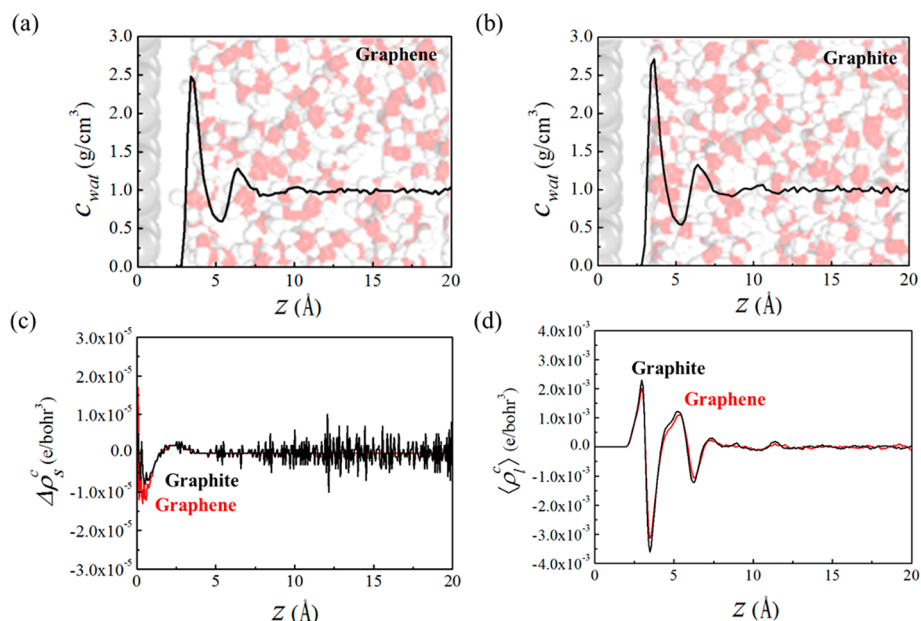


Figure 4. Local water concentration along the z -direction: (a) c_{wat} for graphene–water interface and (b) c_{wat} for graphite–water interface, both of which show a well-defined layering tendency. (c) The in-plane averaged solid charge density difference, $\Delta\rho_s^z$, shows that electrons are polarized at the interface, developing a surface dipole upon the response of the liquid dipolar field. Here, a more negative value corresponds to more electrons. (d) The in-plane and ensemble averaged liquid charge density $\langle\rho_l^z\rangle$ shows that interfacial water layers develop a dipolar field originating from the water molecular orientations at the interface. Graphene and graphite cases are shown in red and black, respectively.

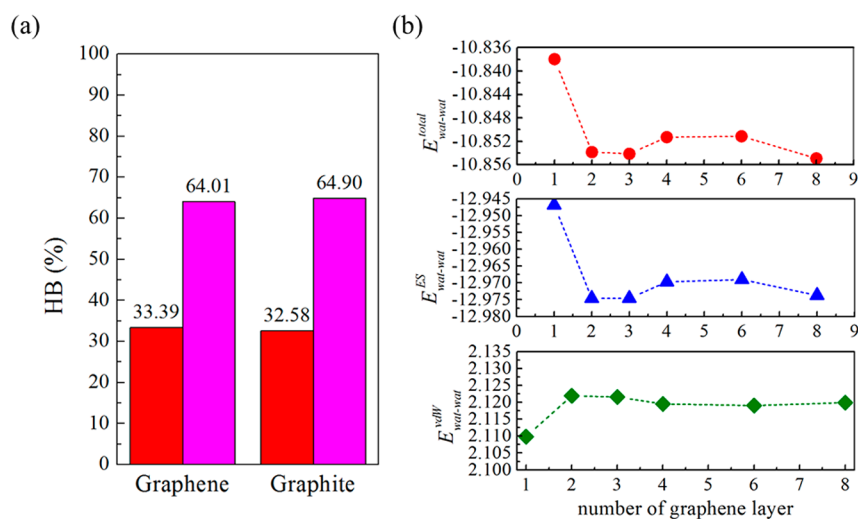


Figure 5. (a) Hydrogen bond (HB) donor analysis of the first water layer at the graphene–water interface (left) and the graphite–water interface (right). There are more double donor (DD) species (magenta) than single donor (SD) species (red), and the population of DD slightly higher for the graphite case than the graphene case. Data shown here are from the SPC/E model, and data from TIP3P-Ew are shown in Figure S6; both sets of data are virtually identical. (b) Change of water–water intermolecular interaction energy (per molecule) as a function of the number of graphene layers. As the number of graphene layer increases, the water–water interaction becomes more stabilized (red circle), via the more developed HB, which appears as an increased electrostatic interaction (blue triangle), whereas vdW repulsion slightly destabilizes water–water interaction (green diamond).

with the decrease of θ_{CA} , i.e., the surface becomes less hydrophobic. These values show a saturating behavior after the number of layers becomes more than 3–4. This implies that graphene wetting is mainly influenced by the vdW interaction at the interface because the vdW interaction shows a similar saturation behavior upon increasing the number of graphene layers beyond the vdW interaction length scale of ~ 10 Å.¹⁹ Indeed, when W_{ad} is compared to the calculated $-E_{\text{int}}^{\text{vdW}}/S$, almost the same trend is observed, as shown in Figure S6.

On the basis of our theoretical contact angle of $\theta_{\text{CA}} = 80^\circ$, we find that the experimental values of 84 – 86° measured by Fowkes¹⁰ and Morcos¹¹ are more convincing than other experimental measurements reporting much smaller values spanning from $\sim 30^\circ$ to 80° .^{12,13} Furthermore, the slightly larger experimental values than the theoretical value could be attributed to the graphite atomic vacancies, which increase the contact angle by losing vdW interacting pairs.

Water Structure and Dynamics at the Interface. From the final MD trajectories, we obtain full atomistic level of information

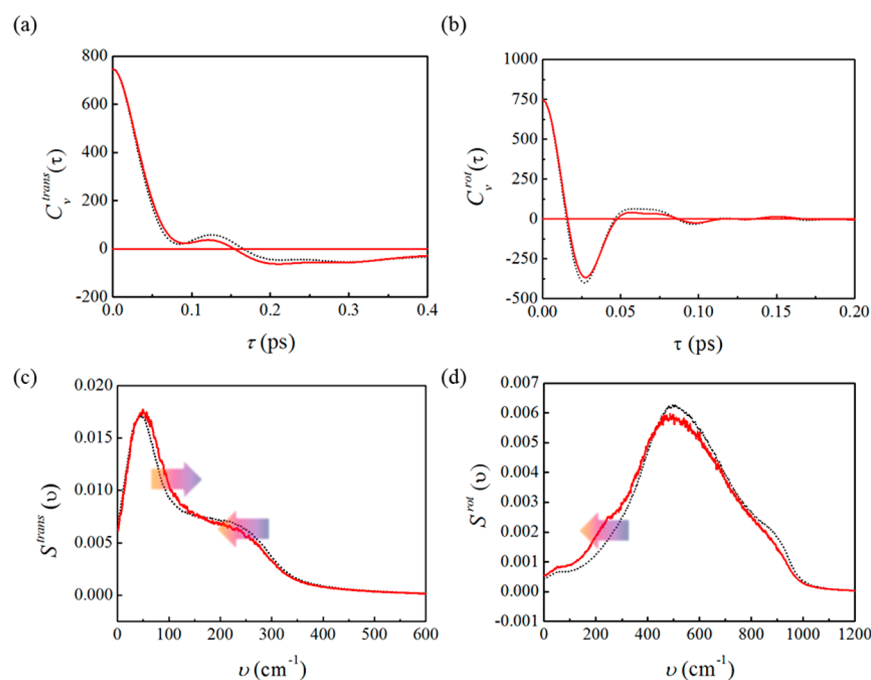


Figure 6. Velocity autocorrelation function (VACF) of the first water layer at the graphene–water interface for (a) translational velocities, $C_v^{\text{trans}}(t)$, and (b) rotational velocities, $C_v^{\text{rot}}(t)$. The Fourier transforms of the functions plotted in panels a and b lead to the power spectra of (c) translational motion, $S_v^{\text{trans}}(\nu)$, and (d) rotational motion, $S_v^{\text{rot}}(\nu)$, respectively. VACF and power spectra of the interfacial water are shown in red solid line, and those of the bulk water are shown in black dotted line for comparison. Data shown here are from the SPC/E model, and the data from TIP3P-Ew are shown in Figure S7; virtually no difference is found between these results.

regarding the liquid structure at the interface. Figure 4a,b show the local concentration of water, c_{wat} , along the surface normal direction (chosen as z -direction) for the cases of graphene monolayer and graphite (which is modeled using 8 layers of graphene). As is widely known from previous studies,^{43,44} we find that a layered structure is developed at the interface; the first and second layers are well-defined, whereas the third layer is rather unclear; further from the interface, c_{wat} converges to the bulk value of 1 g/cm³ ($z > 14$ Å from the surface). We further find the layering tendency becomes more enhanced for graphite rather than graphene, e.g., the first peak intensities are 2.7 g/cm³ and 2.5 g/cm³ for graphite and graphene, respectively. This difference is ascribed to the stronger solid–liquid interfacial interaction energy with the higher value of W_{ad} for graphite.

In Figure 4c, the in-plane averaged charge density difference of the solid surface, $\Delta\rho_s^z$, is calculated from DFT results, where the more negative sign indicates the greater electron density. At the interface, we found that electrons of the graphene/graphite are noticeably polarized toward the water phase as an electrostatic response to the solvent potential, denoted as a $\langle V_{\text{MM}}^{\text{ES}} \rangle$ in eq 1. Indeed, as shown in Figure 4d, the liquid charge distribution, which is also in-plane averaged, $\langle \rho_l^z \rangle$, shows approximately twice the positive-to-negative charge fluctuations along the z -direction (corresponding to the first and second water layers, respectively); these fluctuations develop an interfacial dipole that polarizes the electron density of the solid surface. We note that $\langle \rho_l^z \rangle$ in our simulation is entirely due to the dipolar reorganization of the liquid medium. Thus, the positive-to-negative charge fluctuating behavior originates from the average direction of the molecular dipole of water molecules at the interface, implying that the hydrogen atoms tend to be directed toward the surface at the equilibrium state. This observation can be related to the previous DFT results on

the water monomer binding to the graphene, showing the interaction via hydrogen head is more stable than the interaction via oxygen head.⁴⁵

To gain further insight on the intermolecular water structure at the interface, we analyze hydrogen bonds (HB) among water molecules in the first layer. We define HB using the geometrical criteria having an intermolecular O...O distance shorter than 3.5 Å, and an angle $\angle\text{O-H}\cdots\text{O}$ no greater than 30°.⁴⁶

As shown in Figure 5a and Figure S7, we find that ~65% of the interfacial water molecules have saturated HBs, denoted as double-donor (DD) species, while ~35% of the interfacial water molecules have one broken HB, denoted as single-donor (SD) species. We further find that the population of DD species is slightly larger for graphite than for graphene.

Together with the relative change of c_{wat} , $\Delta\rho_s^z$, and $\langle \rho_l^z \rangle$ discussed above, we conclude that

1. stronger solid–liquid interfacial interaction not only enhances the hydrophilicity of the surface, but also increases the c_{wat} at the first shell,
2. which helps to develop more complete HB networks among the interfacial waters and increase the dipole strength at the interface, and, as a result,
3. electrons of the solid surface are more polarized toward the liquid phase.

This mechanism suggests that the interfacial electrostatic interaction and the intermolecular interaction among waters at the interface can also be enhanced for the more hydrophilic surface, although the increase of interfacial vdW interaction is still the dominant factor determining the surface hydrophilicity.

To check this hypothesis, we investigate the trend of nonbond interaction energies from MD simulations as a function of graphene layers in Figure 5b. As the number of graphene layer increases (i.e., as the surface becomes less

hydrophobic), we find an increase of water–water attractions that provides an additional stabilization energy to the interfacial water molecules and thereby further increases the surface wettability. We also find that the enhanced water–water interaction is caused by the increase of intermolecular electrostatic attraction (because of more developed hydrogen bonds), whereas the vdW contribution increases the intermolecular repulsions (because of the increase of local density).

To understand the dynamics of interfacial waters, we analyzed the velocity autocorrelation functions (VACFs) of the water molecules at the first layer in contact with the graphene surface in Figure 6 (the graphite surface case is shown in Figure S8, which shows only a marginal difference). We calculated VACF for the center-of-mass (COM) translational velocities, $C_v^{\text{trans}}(t)$ and for the COM rotational velocities $C_v^{\text{rot}}(t)$, by decomposing the atomic velocities into molecular translational part and rotational part (Figure 6a,b). We then obtained the corresponding power spectra, $S^{\text{trans}}(\nu)$ and $S^{\text{rot}}(\nu)$ by Fourier transforming $C_v^{\text{trans}}(t)$ and $C_v^{\text{rot}}(t)$, respectively (Figure 6c,d).

$S^{\text{trans}}(\nu)$ shows two representative bands as a peak at ~ 50 cm^{-1} and a shoulder at 250 cm^{-1} ; the peak at ~ 50 cm^{-1} is related to the intermolecular bending motions between $\text{O}\cdots\text{O}\cdots\text{O}$ of the hydrogen bonded water molecules,⁴⁷ and the shoulder at 250 – 300 cm^{-1} is related to the longitudinal $\text{O}\cdots\text{O}$ stretching mode between intermolecular HB pairs.^{48,49} Compared with the power spectrum of the bulk water, we find that the peak at ~ 50 cm^{-1} shows a slight blue-shift, whereas the shoulder at ~ 250 cm^{-1} shows a slight red-shift. In terms of the discontinuity of HB network at the interface, the weakened $\text{O}\cdots\text{O}$ stretching at the less rigid HB network (appeared as a red-shift) can be easily rationalized, whereas the more restricted three-body bending motion at the interface (appeared as a blue-shift) is rather counterintuitive. We believe that this behavior is caused by the increased water density and layering tendency at the interface, which is likely to be related to the decrease of the translational diffusion constant at the interface (Table 2).

Table 2. Translational (D^{trns}) and Rotational Diffusion Coefficients (D^{rot}) of the First Water Layer at the Graphene/Graphite–Water Interface Compared with Bulk Values^a

	bulk water	interfacial water @ graphene	interfacial water @ graphite
D^{trns}	2.80	2.41	2.38
D^{rot}	0.17	0.21	0.20
$D^{\text{tot}} (= D^{\text{trns}} + D^{\text{rot}})$	2.97	2.62	2.58
S^{trns}	50.58	50.69	50.47
S^{rot}	10.68	11.82	11.78
$S^{\text{tot}} (= S^{\text{trns}} + S^{\text{rot}})$	61.26	62.51	62.25

^aTranslational (S^{trns}) and rotational entropies (S^{rot}) are also estimated using 2PT analysis. Units are 10^{-5} cm^2/s for diffusion constants and $\text{J mol}^{-1} \text{K}^{-1}$ for entropy values.

In the case of $S^{\text{rot}}(\nu)$, the interfacial water shows a red-shifting tendency for the low frequency librational bands of peak at ~ 520 cm^{-1} and a shoulder at ~ 1000 cm^{-1} .^{50,51} This can also be understood in terms of the discontinuity of HB network providing a less rigid environment to the water molecules at the interface, thereby suppressing the backscattering, as shown in

$C_v^{\text{rot}}(t)$. This leads to the increase of the rotational diffusion constant at the interface (Table 2).

To connect our understanding on the water dynamics at the interface to the surface wettability, we performed 2PT analysis only for the water molecules at the first layer contacting with the graphene (or graphite) surface. Overall, the calculated entropy values of the interfacial water molecules are in a very similar range to the bulk value (Table 2), suggesting no formation of ice-like structure with low entropy at the graphene/graphite interface.⁵² However, one can also discuss slight differences of the interfacial water entropy from the bulk values; for example, in terms of translational entropy, interfacial water of graphene system shows increase of 0.09 J/mol/K , whereas interfacial water shows a decrease of 0.12 J/mol/K in the graphite system. More dominant changes are shown from the case of rotational entropy; the rotational entropy increases at both the graphene and graphite system by 1.14 J/mol/K and 1.01 J/mol/K , respectively. Finally, the total entropy is estimated to increase by 1.25 J/mol/K (0.99 J/mol/K) at the graphene (graphite) interface, which stabilizes the interface and thereby helps to increase surface wettability.

In this study, we proposed a multiscale approach to quantitatively predict a theoretical contact angle using our recently developed mean-field QM/MM method, DFT-CES. By bridging the quantum Hamiltonian describing the electronic and structural change of the solid part and the classical Hamiltonian describing the structural and dynamical change of the liquid part, we can accurately compute the solid–liquid interfacial free energy that is directly converted into the contact angle value. In particular, we demonstrated that our method describes the single water binding to the solid surface and solid–liquid interfacial free energy at an equal footing. This enables a systematic multiscale approach in which one can optimize the interfacial vdW parameters from the most reliable QM calculation for the single water binding; these parameters are then transferred to the investigation of solid–liquid interface using DFT-CES.

Using the graphene and graphite cases as examples, we calculated the theoretical water contact angle values as $\sim 88^\circ$ and $\sim 80^\circ$, respectively, which not only were in good agreement with the reliable experimental values but also suggested the theoretical bound for the contact angle of ideally clean surfaces. From the detailed analyses about the electronic change of the solid and the structural and dynamical changes of the liquid at the interface, we also found the following microscopic changes at the solid–liquid interface that increase the surface hydrophilicity upon the increase of graphene layers:

- the primary origin of enhanced hydrophilicity is the increase of vdW pair (in similar to the previous understanding);
- however, the increase of vdW pairs also leads to a denser water layer at the interface, which further (enthalpically) stabilizes the interfacial water layer by allowing more HBs (further increases the surface hydrophilicity).
- In addition, dynamics of the interfacial water show a suppressed translational diffusion as well as an enhanced rotational diffusion, leading to the entropic stabilization of the interfacial water and increasing the surface hydrophilicity.

As shown above, having full atomistic descriptions of the solid and liquid parts, our multiscale simulation approach provides a microscopic level of understanding on the wetting

behavior of the surface. We thus anticipate that our proposed multiscale approach can be widely applied in exploring many intriguing surface wetting phenomena at the atomistic level, e.g., nanoscale wetting behavior and wetting transparency.

■ ASSOCIATED CONTENT

📄 Supporting Information

The Supporting Information is available free of charge on the ACS Publications website at DOI: 10.1021/acs.jpcllett.8b00466.

Figures S1–S7 (PDF)

■ AUTHOR INFORMATION

Corresponding Authors

*E-mail: hklm@kangwon.ac.kr (H.-K.L.) and

*E-mail: linus16@kaist.ac.kr (H.K.).

ORCID

Hyung-Kyu Lim: 0000-0002-2403-2766

Hyunjun Kim: 0000-0001-8261-9381

Notes

The authors declare no competing financial interest.

■ ACKNOWLEDGMENTS

This work was supported by the Nanomaterial Technology Development Program (Grant 2016M3A7B4025414) through the National Research Foundation of Korea (NRF) funded by the Ministry of Science and ICT, and also by the New & Renewable Energy Core Technology Program of the Korea Institute of Energy Technology Evaluation and Planning (KETEP) granted financial resource from the Ministry of Trade, Industry & Energy, Republic of Korea (20153030031720).

■ REFERENCES

- (1) Kim, G. T.; Gim, S. J.; Cho, S. M.; Koratkar, N.; Oh, I. K. Wetting-Transparent Graphene Films for Hydrophobic Water-Harvesting Surfaces. *Adv. Mater.* **2014**, *26*, 5166–5172.
- (2) Fürstner, R.; Barthlott, W.; et al. Wetting and Self-Cleaning Properties of Artificial Superhydrophobic Surfaces. *Langmuir* **2005**, *21*, 956–961.
- (3) Thomas, R. R.; Brusica, V. A.; Rush, B. M. Correlation of Surface Wettability and Corrosion Rate for Benzotriazole-Treated Copper. *J. Electrochem. Soc.* **1992**, *139* (3), 678–685.
- (4) Kochan, J.; Wintgens, T.; Hochstrat, R.; Melin, T. Impact of Wetting Agents on the Filtration Performance of Polymeric Ultrafiltration Membranes. *Desalination* **2009**, *241*, 34–42.
- (5) Wang, L.; Xiao, F. S. The Importance of Catalyst Wettability. *ChemCatChem* **2014**, *6* (11), 3048–3052.
- (6) Horowitz, G. I.; Martinez, O.; Cukierman, A. L.; Cassanello, M. C. Effect of the Catalyst Wettability on the Performance of a Trickle-Bed Reactor for Ethanol Oxidation as a Case Study. *Chem. Eng. Sci.* **1999**, *54*, 4811–4816.
- (7) Schrader, M. E. Ultrahigh-Vacuum Techniques in the Measurement of Contact Angles. 5. LEED Study of the Effect of Structure on the Wettability of Graphite. *J. Phys. Chem.* **1980**, *84*, 2774–2779.
- (8) Li, Z.; Wang, Y.; Kozbial, A.; Shenoy, G.; Zhou, F.; McGinley, R.; Ireland, P.; Morganstein, B.; Kunkel, A.; Surwade, S. P.; Li, L.; Liu, H. Effect of Airborne Contaminants on the Wettability of Supported Graphene and Graphite. *Nat. Mater.* **2013**, *12*, 925–931.
- (9) Reuter, K.; Stampfl, C.; Ganduglia-Pirovano, M. V.; Scheffler, M. Atomistic Description of Oxide Formation on Metal Surfaces: the Example of Ruthenium. *Chem. Phys. Lett.* **2002**, *352*, 311–317.
- (10) Fowkes, F. M.; Harkins, W. D. The State of Monolayers Adsorbed at the Interface Solid—Aqueous Solution. *J. Am. Chem. Soc.* **1940**, *62*, 3377–3386.

(11) Morcos, I. Surface Tension of Stress-Annealed Pyrolytic Graphite. *J. Chem. Phys.* **1972**, *57* (4), 1801.

(12) Tadros, M. E.; Hu, P.; Adamson, A. W. Adsorption and Contact Angle Studies: I. Water On Smooth Carbon, Linear Polyethylene, and Stearic Acid-Coated Copper. *J. Colloid Interface Sci.* **1974**, *49*, 184.

(13) Luna, M.; Colchero, J.; Baró, A. M. Study of Water Droplets and Films on Graphite by Noncontact Scanning Force Microscopy. *J. Phys. Chem. B* **1999**, *103*, 9576.

(14) Silvestrelli, P. L. Van der Waals Interactions in Density Functional Theory by Combining the Quantum Harmonic Oscillator-Model with Localized Wannier Functions. *J. Chem. Phys.* **2013**, *139*, 054106.

(15) Tkatchenko, A.; Scheffler, M. Accurate Molecular van der Waals Interactions from Ground-State Electron Density and Free-Atom Reference Data. *Phys. Rev. Lett.* **2009**, *102*, 073005.

(16) Grimme, S.; Antony, J.; Ehrlich, S.; Krieg, S. A Consistent and Accurate Ab Initio Parametrization of Density Functional Dispersion Correction (DFT-D) for the 94 Elements H–Pu. *J. Chem. Phys.* **2010**, *132*, 154104.

(17) Grimme, S.; Ehrlich, S.; Goerigk, L. Effect of The Damping Function In Dispersion Corrected Density Functional Theory. *J. Comput. Chem.* **2011**, *32*, 1456.

(18) Berland, K.; Cooper, V. R.; Lee, K.; Schröder, E.; Thonhauser, T.; Hyldgaard, P.; Lundqvist, B. I. van der Waals forces in Density Functional Theory: A Review of the Vdw-DF Method. *Rep. Prog. Phys.* **2015**, *78*, 066501.

(19) Kim, M.; Kim, W. J.; Lee, E. K.; Lébêgue, S.; Kim, H. Recent Development of Atom-Pairwise Van Der Waals Corrections for Density Functional Theory: From Molecules to Solids. *Int. J. Quantum Chem.* **2016**, *116*, 598–607.

(20) Driskill, J.; Vanzo, D.; Bratko, D.; Luzar, A. Wetting Transparency of Graphene in Water. *J. Chem. Phys.* **2014**, *141*, 18C517.

(21) Raj, R.; Maroo, S. C.; Wang, E. N. Wettability of Graphene. *Nano Lett.* **2013**, *13* (4), 1509.

(22) Shih, C. J.; Wang, Q. H.; Lin, S.; Park, K. C.; Jin, Z.; Strano, M. S.; Blankschtein, D. Breakdown in the Wetting Transparency of Graphene. *Phys. Rev. Lett.* **2012**, *109*, 176101.

(23) Scocchi, G.; Sergi, D.; D'Angelo, C.; Ortona, A. Wetting and Contact-Line Effects for Spherical and Cylindrical Droplets on Graphene Layers: A Comparative Molecular-Dynamics Investigation. *Phys. Rev. E* **2011**, *84*, 061602.

(24) Schimmele, L.; Dietrich, S. Line Tension and the Shape of Nanodroplets. *Eur. Phys. J. E: Soft Matter Biol. Phys.* **2009**, *30*, 427.

(25) Werder, T.; Walther, J. H.; Jaffe, R. L.; Halicioglu, T.; Noca, F.; Koumoutsakos, P. Molecular Dynamics Simulation of Contact Angles of Water Droplets in Carbon Nanotubes. *Nano Lett.* **2001**, *1* (12), 697–702.

(26) Werder, T.; Walther, J. H.; Jaffe, R. L.; Halicioglu, T.; Koumoutsakos, P. On The Water-Carbon Interaction for Use in Molecular Dynamics Simulations of Graphite and Carbon Nanotubes. *J. Phys. Chem. B* **2003**, *107*, 1345–1352.

(27) Taherian, F.; Marcon, V.; van der Vegt, N. F. A.; Leroy, F. What is the Contact Angle of Water on Graphene? *Langmuir* **2013**, *29*, 1457–1465.

(28) Lim, H. K.; Lee, H. K.; Kim, H. A Seamless Grid-Based Interface for Mean-Field QM/MM Coupled with Efficient Solvation Free Energy Calculations. *J. Chem. Theory Comput.* **2016**, *12*, S088–S099.

(29) Lin, S. T.; Blanco, M.; Goddard, W. A. The Two-Phase Model for Calculating Thermodynamic Properties of Liquids from Molecular Dynamics: Validation for the Phase Diagram of Lennard-Jones Fluids. *J. Chem. Phys.* **2003**, *119* (22), 11792.

(30) Pascal, T. A.; Schärf, D.; Jung, Y.; Kühne, T. D. On the Absolute Thermodynamics of Water from Computer Simulations: A Comparison of First-Principles Molecular Dynamics, Reactive and Empirical Force Fields. *J. Chem. Phys.* **2012**, *137*, 244507.

(31) Lin, S. T.; et al. Two-Phase Thermodynamic Model for Efficient and Accurate Absolute Entropy of Water from Molecular Dynamics Simulations. *J. Phys. Chem. B* **2010**, *114* (23), 8191–8198.

(32) Pascal, T. A.; Lin, S. T.; Goddard, W. A., III Thermodynamics of Liquids: Standard Molar Entropies and Heat Capacities of Common Solvents from 2PT Molecular Dynamics. *Phys. Chem. Chem. Phys.* **2011**, *13*, 169–181.

(33) Navascues, G.; Berry, M. V. The Statistical Mechanics of Wetting. *Mol. Phys.* **1977**, *34*, 649–664.

(34) Giannozzi, P.; Baroni, S.; Bonini, N.; Calandra, M.; Car, R.; Cavazzoni, C.; Ceresoli, D.; Chiarotti, G. L.; Cococcioni, M.; Dabo, I.; Dal Corso, A.; Fabris, S.; Fratesi, G.; Gironcoli, S.; Gebauer, R.; Gerstmann, U.; Gougoussis, C.; Kokalj, A.; Lazzeri, M.; Samos, L. M.; Marzari, N.; Mauri, F.; Mazzarello, R.; Paolini, S.; Pasquarello, A.; Paulatto, L.; Sbraccia, C.; Scandolo, S.; Sclauzero, G.; Seitsonen, A. P.; Smogunov, A.; Umari, P.; Wentzcovitch, R. M. Quantum ESPRESSO: A Modular and Open-Source Software Project for Quantum Simulations of Materials. *J. Phys.: Condens. Matter* **2009**, *21*, 395502.

(35) Perdew, J. P.; Burke, K.; Ernzerhof, M. Generalized Gradient Approximation Made Simple. *Phys. Rev. Lett.* **1996**, *77* (18), 3865–3868.

(36) Blöchl, P. E. Projector Augmented-Wave Method. *Phys. Rev. B: Condens. Matter Mater. Phys.* **1994**, *50*, 17953.

(37) Hamada, I.; Otani, M. Comparative van der Waals Density-Functional Study of Graphene on Metal Surfaces. *Phys. Rev. B: Condens. Matter Mater. Phys.* **2010**, *82*, 153412.

(38) Plimpton, S. Fast Parallel Algorithms for Short-Range Molecular Dynamics. *J. Comput. Phys.* **1995**, *117*, 1–19.

(39) Berendsen, H. J. C.; Grigera, J. R.; Straatsma, T. P. The Missing Term in Effective Pair Potentials. *J. Phys. Chem.* **1987**, *91*, 6269–6271.

(40) Ma, J.; Michaelides, A.; Alfe, D.; Schimka, L.; Kresse, G.; Wang, E. Adsorption and Diffusion of Water on Graphene From First Principles. *Phys. Rev. B: Condens. Matter Mater. Phys.* **2011**, *84*, 033402.

(41) Hamada, I. Adsorption of water on graphene: A van der Waals Density Functional Study. *Phys. Rev. B: Condens. Matter Mater. Phys.* **2012**, *86*, 195436.

(42) Price, D. J.; Brooks, C. L., III A modified TIP3P water potentials for simulation with Ewald summation. *J. Chem. Phys.* **2004**, *121* (20), 10096–10103.

(43) Walther, J. H.; Jaffe, R.; Halicioglu, T.; Koumoutsakos, P. Carbon Nanotubes in Water: Structural Characteristics and Energetics. *J. Phys. Chem. B* **2001**, *105*, 9980–9987.

(44) Zangi, R. Water Confined to a Slab Geometry: a Review of Recent Computer Simulation Studies. *J. Phys.: Condens. Matter* **2004**, *16*, S5371–S5388.

(45) Voloshina, E.; Usvyat, D.; Schütz, M.; Dedkov, Y.; Paulus, B. On The Physisorption of Water on Graphene: A CCSD(T) Study. *Phys. Chem. Chem. Phys.* **2011**, *13*, 12041–12047.

(46) Luzar, A.; Chandler, D. Hydrogen-Bond Kinetics in Liquid Water. *Nature* **1996**, *379* (4), 55.

(47) Pal, S.; Balasubramanian, S.; Bagchi, B. Dynamics of Bound and Free Water in an Aqueous Micellar Solution: Analysis of the Lifetime and Vibrational Frequencies of Hydrogen Bonds at a Complex Interface. *Phys. Rev. E: Stat. Phys., Plasmas, Fluids, Relat. Interdiscip. Top.* **2003**, *67*, 061502.

(48) Deshmukh, S. A.; Kamath, G.; Baker, G. A. The Interfacial Dynamics of Water Sandwiched between Graphene Sheets are Governed by the Slit Width. *Surf. Sci.* **2003**, *609*, 129–139.

(49) Balucani, U.; Brodholt, J. P.; Vallauri, R. Analysis of the Velocity Autocorrelation Function of Water. *J. Phys.: Condens. Matter* **1996**, *8*, 6139.

(50) Cicero, G.; Grossman, J. C.; Schwegler, E.; Gygi, F.; Galli, G. Water Confined in Nanotubes and between Graphene Sheets: A First Principle Study. *J. Am. Chem. Soc.* **2008**, *130*, 1871.

(51) Praprotnik, M.; Janezic, D.; Mavri, J. Temperature Dependence of Water Vibrational Spectrum: A Molecular Dynamics Simulation Study. *J. Phys. Chem. A* **2004**, *108*, 11056.

(52) Qiu, Y.; Lupi, L.; Molinero, V. Is Water at the Graphite Interface Vapor-like or Ice-like? *J. Phys. Chem. B* **2018**, DOI: 10.1021/acs.jpcc.7b11476.